A&A, 706, A262 (2026)
https://doi.org/10.1051/0004-6361/202557731

Astronomy & Astrophysics

Rotational evolution of slow–rotator sequence stars

II. Modeling the wind braking and rotational coupling in the entire mass range of solar-like stars

F. Spada[1,★] and A. C. Lanzafame[1,2]

[1] Università di Catania, Dipartimento di Fisica e Astronomia, Sezione Astrofisica, Via S. Sofia 78, 95123 Catania, Italy
[2] INAF-Osservatorio Astrofisico di Catania, Via S. Sofia 78, 95123 Catania, Italy

Received 17 October 2025 / Accepted 8 December 2025

ABSTRACT

In recent years, ground- and space-based photometric surveys have characterized the rotational evolution of solar-like stars to an unprecedented level of detail. In this work we focus on the slow–rotator sequence, an emergent feature recognizable in the color–period diagram of Galactic open clusters. Understanding the evolution of this sequence is a promising avenue for formulating a robust rotation period–mass–age relation, which can be used to estimate stellar ages. Our model of the rotational evolution of stars on the slow–rotator sequence takes into account magnetized wind braking and rotational decoupling between the radiative interior and the convective envelope. This decoupling naturally develops as the internal redistribution of angular momentum lags behind the loss of angular momentum at the stellar surface, and is parameterized in the model by a rotational coupling timescale. Using data from the literature on rotation and membership of stars in a selection of open clusters, aged between 100 Myr and 4 Gyr, we constrain the mass dependence of the two competing processes of wind braking at the surface and angular momentum transport in the interior. Consistent with our previous findings, our best-fitting model requires a mass-dependent coupling timescale; this result is insensitive to the details of the wind braking model used. We show that the mass dependence of the coupling timescale follows a broken power law in the entire solar-like mass range (0.4−1.25 $M_\odot$), with the exponent change occurring at ≈0.6 $M_\odot$. At the same time, our approach can be used to infer semi-empirically the mass dependence of the wind braking model that best fits the observational constraints. Based on our findings, we propose a novel wind braking law with a particularly simple mass term, directly proportional to the moment of inertia of the convective envelope of the star.

Key words. stars: evolution – stars: late-type – stars: rotation – open clusters and associations: general

1. Introduction

In stars with outer convective envelopes, mass loss from a magnetized stellar wind, powered by dynamo action, results in a braking torque that drives a significant rotational evolution. The surface rotation period of a 1 $M_\odot$ star, for instance, decreases by a factor of ≈25 over the approximately 5 Gyr interval between the zero-age main sequence (ZAMS) and solar age (Barnes et al. 2016). In a similar fashion, stars with masses between 0.4 and 1.25 $M_\odot$ undergo a "solar-like" rotational evolution.

The most stringent observational constraints on solar-like rotational evolution come from surface rotation periods measured via photometric monitoring for stars that are members of coeval populations of known age, such as Galactic open clusters. Observational color–period diagrams of open clusters, in particular, provide snapshots of the rotational state of stars of different mass, inferred from the observational proxy of their photometric color, at approximately the same age, which can be independently and reliably estimated from isochrone fitting (e.g., Demarque & Larson 1964).

In a seminal paper, (Barnes 2003) pointed out that a sequence of comparatively slow rotators gradually emerges in the color–period diagram of clusters aged between 30 and 600 Myr, and that the timescale for transition from fast- to slow-rotator status is mass-dependent, i.e., solar-type stars are already on the sequence by ≈100 Myr, while stars of later spectral type converge onto it at progressively later ages. Although the transition from fast to slow rotator is still not fully understood (see, e.g., Barnes 2010; Matt et al. 2012; Brown 2014; Lanzafame et al. 2019), the details of the underlying process are mostly forgotten after the first ≈100 Myr. The subsequent evolution of the slow–rotator sequence is remarkably regular and, somewhat analogously to the main sequence in the classical color–magnitude diagram, encodes key information on the solar-like rotational evolution process as a whole.

The emergent properties of the slow–rotator sequence (i.e., its overall evolution and its mass dependence) place strong constraints on two key physical processes whose theoretical understanding remains elusive, namely, the removal of angular momentum from the surface mediated by the magnetized stellar wind and the transport of angular momentum in the stellar interior. The former, usually referred to as (magnetized) wind braking, is the main driver of the rotational evolution of solar-like stars during their main sequence lifetime, while the latter, remarkably, has second-order yet observable consequences, and thus provides a window into the physics of stellar interiors.

Wind braking in solar-like stars has been known observationally and, at least in broad terms, understood theoretically, for more than fifty years (Kraft 1967; Skumanich 1972; Schatzman 1962; Weber & Davis 1967; Kawaler 1988). The general picture established in these early works is still accepted today: the wind

★ Corresponding author: federico.spada@gmail.com

effectively applies on the star a braking torque, which is proportional to the mass loss rate and to the surface rotation rate and, crucially, is greatly amplified by the fact that the wind outflows are dominated by the dynamo magnetic fields up to several stellar radii from the surface. This basic mechanism is responsible for the observed spin-down of cool stars, which, to the lowest order of approximation, is captured by the Skumanich (1972) law: $P_{\rm rot} \propto \sqrt{\rm age}$.

Large rotation period surveys – based on observations from Kepler, K2, and the Transiting Exoplanet Survey Satellite (TESS) – together with Gaia-informed cluster ages, have produced dense rotation–age–mass data sets spanning from tens of Myr to several Gyr (e.g., Van-Lane et al. 2025, and references therein), revealing a rich set of features that simple spin-down relations, such as the Skumanich law, cannot fit. For instance, the spin-down mass dependence cannot be fully factored out from the age dependence (Meibom et al. 2009, 2011; Lanzafame & Spada 2015), it may anomalously slow down ("stall") at certain ages (Curtis et al. 2020), and it may even shut down beyond solar age (van Saders et al. 2016; Metcalfe et al. 2025). The torque normalization and its scaling relations with stellar rotation, mass, and other physical parameters required to reproduce the observed features of rotational evolution are the subject of active research, and several wind braking laws have been proposed in the literature (e.g., Krishnamurthi et al. 1997; Matt et al. 2012; Reiners & Mohanty 2012; Matt et al. 2015; Garraffo et al. 2018; Spada & Lanzafame 2020).

Measurement of the rotation profile of the solar interior via helioseismic inversion (Christensen-Dalsgaard & Schou 1988; Schou et al. 1998), on the other hand, indirectly constrains the transport of angular momentum in the interior of solar-like stars (e.g., Eggenberger et al. 2005). In particular, the nearly uniform rotation of the solar interior implies that efficient angular momentum redistribution must occur during the main sequence. An independent confirmation comes from asteroseismic inversions in subgiants and red giant stars, which reveal that the cores of these stars rotate faster than the envelopes, but much more slowly than predicted by models without efficient angular momentum transport, again implying a strong coupling between core and envelope during evolution (e.g., Mosser et al. 2012; Cantiello et al. 2014; Deheuvels et al. 2014; Fuller et al. 2014; Spada et al. 2016; Eggenberger et al. 2019; Deheuvels et al. 2020; Moyano et al. 2023).

Standard models with only hydrodynamic processes fail to match asteroseismic constraints (e.g., Pinsonneault et al. 1989; Eggenberger et al. 2005). Including magnetic fields or internal gravity waves improves the agreement, but the exact combination and efficiency of these mechanisms remain uncertain (Charbonneau & MacGregor 1993; Ruediger & Kitchatinov 1996; Charbonnel & Talon 2005; Oglethorpe & Garaud 2013; Aerts et al. 2019).

In summary, in spite of considerable theoretical and observational progress, a comprehensive physical picture of either wind braking or rotational coupling in solar-like stars is still lacking. Building on previous work, in this paper we focus in particular on improving the mass-scaling of these two processes, based on the constraints that can be extracted from the observed slow–rotator sequence.

A key feature of our modeling paradigm is a two-zone description of the rotation profile in the interior of the star (MacGregor & Brenner 1991). This simple but versatile approach introduces a differential rotation between the radiative interior and the convective envelope, parametrizing the angular momentum transport with a rotational coupling timescale (e.g., Spada et al. 2011; Gallet & Bouvier 2013, 2015). A short coupling timescale keeps a star rotating as a solid body essentially at all times, while a longer timescale allows for some angular momentum to be temporarily stored in the radiative interior, to resurface later and temporarily offset the evolution toward longer rotation periods. Such non-monotonic rotational evolution of the surface rotation periods suffices to capture quantitatively the observed stalled magnetic braking (Curtis et al. 2019, 2020; Angus et al. 2020; Gordon et al. 2021; Santos et al. 2025).

In this work, we derive the parametric dependence of the coupling timescale on stellar mass across the full range of stars with solar-like interior structure, confirming and extending the results of Lanzafame & Spada (2015) and Spada & Lanzafame (2020) (hereafter LS15 and SL20, respectively). We find that this dependence is robust to different choices of the wind braking law. We further derive a semi-empirical mass term for the wind braking law and show that its functional behavior is well described by a scaling with a single stellar parameter, namely, the moment of inertia of the convective envelope.

This paper is organized as follows: In Section 2 we discuss the criteria used to construct the data set that we use to constrain our models; in Section 3 we describe the preparation and treatment of the data, the formulation of our rotational evolution model, and our fitting procedure; our results are presented in Section 4, and discussed in Section 5; we summarize our conclusions in Section 6.

Table 1. Parameters of open clusters used in this work.

Name	Main ref.	$E(B-V)$	Age (Gyr)
Pleiades	(1)	0.045 (6)	0.12 (9)
NGC 3532	(2)	0.022 (6)	0.30 (11)
M37	(3)	0.246 (7)	0.50 (12)
Praesepe	(1)	0.027 (6)	0.70 (9)
NGC 6811	(1)	0.047 (7)	1.00 (9)
NGC 6819	(1)	0.1 (8)	2.50 (9)
Ruprecht 147	(1)	0.1 (9)	2.70 (9)
M67	(4), (5)	0.04 (10)	4.00 (13)

Notes. Rotation periods and membership are from main reference. (1) Curtis et al. (2020); (2) Fritzewski et al. (2021); (3) Hartman et al. (2009); (4) Dungee et al. (2022); (5) Gruner et al. (2023); (6) Gaia Collaboration (2018); (7) Godoy-Rivera et al. (2021); (8) Bragaglia et al. (2001); (9) Curtis et al. (2020); (10) Taylor (2007); (11) Fritzewski et al. (2021); (12) Hartman et al. (2009); (13) Gruner et al. (2023).

2. Data

Following up on our previous work (LS15; SL20), we extend our modeling of the slow–rotator sequence to the widest possible domain of applicability. To this end, we fit our models with rotation period data of stars in the mass range 0.4−1.25 $M_\odot$, and in a (nominal) age range of 0.1−4 Gyr. By definition, the two-zone model approach (see Section 3.2) is applicable to stars that have a solar-like interior structure during the main sequence, namely, a sufficiently developed radiative core (which implies the lower limit $M_* \gtrsim 0.35\,M_\odot$) and a sufficiently massive convective envelope (implying $M_* \lesssim 1.3\,M_\odot$). The age range considered, on the other hand, is limited by the occurrence of the slow–rotator sequence in open clusters, as well as the availability of observational data. The youngest cluster in which the slow–rotator sequence is significantly developed is the ≈100 Myr old

Pleiades, while the oldest open cluster for which rotational information is currently available is the ≈4 Gyr old M67. Further restrictions on the applicability of our models may arise from the so-called "weakened magnetic braking" phenomenon (van Saders et al. 2016). We do not attempt to model the influence of metallicity on the rotational evolution of solar-like stars (e.g., Amard & Matt 2020).

Our dataset consists of a compilation of rotation periods, together with membership and photometric information, for stars that are members of open clusters in which the slow–rotator sequence (also known as the "I-sequence", see Barnes 2003) is readily identifiable and well constrained by the available data. The open clusters selected for this work are listed in Table 1, which also includes nominal ages and visual reddening, with their respective references.

Our selection was based on three main criteria: (i) the existence and adequate sampling of the slow–rotator sequence; (ii) dense logarithmically spaced coverage of the 0.1−4 Gyr time span; (iii) richness and quality of the available data (e.g., accurate rotation periods from space-based photometric surveys, reliable membership information). Our selection of open clusters is clearly not the only possible one, nor is it meant to be exhaustive or fully representative of the entire rotational dataset available in the literature to date.

We adopted the de-reddened Gaia $G_{\rm BP} - G_{\rm RP}$ color as our observational proxy of stellar mass. We used Gaia colors from the latest data release (DR3; Andrae et al. 2023; De Angeli et al. 2023) for the stars in each cluster. We applied the de-reddening procedure described in Gaia Collaboration (2018), with the polynomial fit coefficients reported in that paper.

In this work, we do not attempt to address directly the uncertainty on age or on reddening. In particular, we chose not to include the ages of the clusters as free parameters in our fit. The uncertainty of ages is therefore not explicitly taken into account in our fit, but we have verified that age variations within a reasonable range (≈10%) do not affect our results significantly. We will comment further on the robustness of our models to changes in the adopted nominal ages of the clusters in Section 4.3.

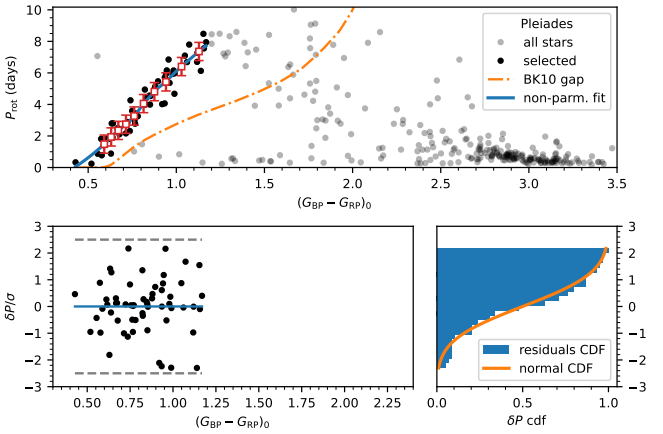

Fig. 1. Non–parametric fitting of slow–rotator sequence of Pleiades. Top panel: color–period diagram; the empirical constraints on slow–rotator sequence extracted from non-parametric fit are shown as empty red squares with error bars. Bottom left: normalized fit residuals; grey dashed lines represent deviations of $\pm 2.5 \times \sigma$ from mean. Bottom right: cumulative distribution of normalized fit residuals compared with that of normal distribution.

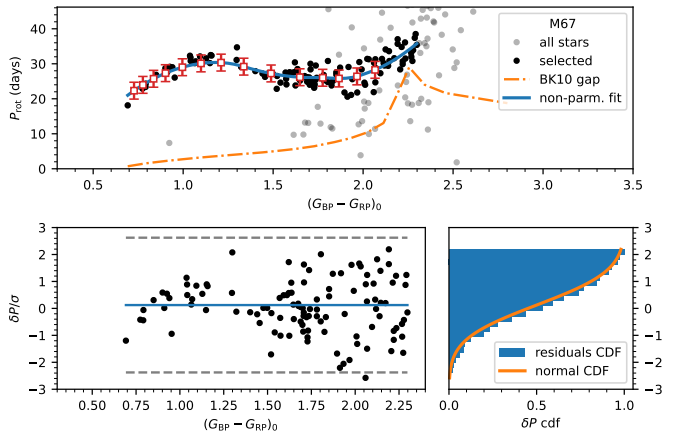

Fig. 2. Same as Figure 1, but for M67.

3. Methods

Our procedure for modeling the slow–rotator sequence consists of two steps. First, for each of the open clusters in our catalog (see Section 2), we identify the stars belonging to the slow–rotator sequence, and from this we determine the empirical color–period relation of the sequence of the cluster by means of a non-parametric fit. After transforming the color into mass by isochrone interpolation, we obtain the empirical mass–period relation of the slow–rotator sequence as a function of age between 0.1 and 4.0 Gyr for the mass range 0.4−1.25 $M_\odot$. In the second step, we use these empirical constraints to fit the parameters of our rotational evolution model. This second fit is based on a standard least-squares approach. The rest of this section provides a detailed description of our methodology.

3.1. Selection of the slow–rotator sequence

To identify the stars belonging to the slow–rotator sequence in a given cluster we adopt the same iterative procedure used in LS15. Starting from an initial selection of candidate members, we obtain an approximate color–period relation on the sequence via a non–parametric fit. The rotation period residuals of the candidate members with respect to the current fit are then evaluated, and stars with residuals larger than 2.5 standard deviations are discarded. This process is repeated until convergence (≲5 iterations are usually sufficient). The standard deviation of the residuals with respect to the converged fit is taken to be representative of the spread of the slow–rotator sequence of that particular cluster. We adopt this converged standard deviation as a measure of the uncertainty in the empirical color–period distribution. Note that both intrinsic spread, astrophysical in origin and spread due to observational errors, are likely to contribute to this uncertainty. Distinguishing the exact source of this spread is not necessary for our purposes, as explained below.

The candidate stars included in the starting guess are those having rotation periods above the empirical "gap curve" of Barnes & Kim (2010) in the color–period diagram. The non-parametric fit is based on the local polynomial regression fit procedure (LOESS; Cleveland et al. 2017), as implemented in the statistical package R. The smoothing parameter of the LOESS fit was adjusted by trial and error, and the final values are between 0.5 and 0.8 for all clusters. In general, we only considered stars with $(G_{\rm BP} - G_{\rm RP})_0 \leq 2.3$, i.e., bluer than the transition to fully convective interiors (except for the Pleiades, see below). Although there is no strong theoretical motivation to expect that

the stars on the slow–rotator sequence should be distributed normally around its middle ridge, as discussed at length in LS15, this procedure is sufficiently robust and accurate to select the sequence members and provide an internally consistent approach to construct a fit of the sequence for each cluster in our sample.

In practice, the identification of the sequence is almost trivial for clusters that have very few or no fast rotators in the $(G_{\rm BP} - G_{\rm RP})_0$ range considered. This is the case for NGC 3532, M37, Praesepe, NGC 6811, NGC 6819, Ruprecht 147. For these clusters, the selection procedure described above is mostly required to address the slow–rotator status in specific color subranges, and to obtain a fit of the slow–rotator sequence, with its associated uncertainty, in a way that is as uniform as possible across the clusters. The Pleiades and M67, on the other hand, deserve some additional comments.

The Pleiades cluster is sufficiently young to have a significant population of fast rotators and "gap" stars into which the slow–rotator sequence merges, and becomes hard to disentangle from, at $(G_{\rm BP} - G_{\rm RP})_0 \gtrsim 1.2$ (see Figure 1). We therefore introduce a cutoff at this color, to ensure that our models are fitted only to bona-fide slow rotators. A similar situation arises for the late K-/early M-type stars in M67, since these stars transition to the slow–rotator sequence with a timescale of the order of a few Gyr (see Figure 2). In this case, however, we obtained a satisfactory selection of the slow–rotator sequence using the iterative procedure based on the non–parametric fit described above, albeit with a converged σ value that is significantly larger than for the other clusters.

Upon convergence, our iterative procedure provides a non-parametric fit and a standard deviation of its residuals, which we adopt as the empirical color–period distribution of the slow–rotator sequence and its uncertainty, respectively, at the nominal age of that cluster. The empirical relations are finally converted from color–period to mass–period by interpolation, using isochrones of solar metallicity and appropriate age extracted from the MIST database (Choi et al. 2016).

3.2. The rotational evolution model

Our rotational evolution model follows the two-zone paradigm (see also LS15; SL20, and references therein). The key assumption of the two-zone model is that, while the radiative interior and the convective envelope of a solar-like star rotate with approximately uniform velocity, a significant rotational gradient can develop at the interface between these two regions (MacGregor & Brenner 1991). In other words, we assume that the rotation profile of a main sequence, solar-like star at any time t can be approximated with a step function, with the transition between the angular velocity of the radiative zone, $\Omega_c(t)$, to that of the convective envelope, $\Omega_e(t)$, located at the bottom of the convective envelope.

The model describes the evolution of Ω_c and Ω_e, taking into account the following physical processes:

- The initial conditions at $t = t_0 \lesssim 1$ Myr assume a fully convective, uniformly rotating star with initial period P_0, i.e., $\Omega_c(t_0) = \Omega_e(t_0) = 2\pi/P_0$; as soon as a radiative core starts to form (within a few to tens of Myr since the birth line, depending on the mass of the star), Ω_c and Ω_e can assume distinct values.
- According to the disk-locking paradigm (Koenigl 1991), we assume that the magnetic interaction of the young star with its circumstellar disk keeps the angular velocity of the convective envelope constant for the lifetime of the disk ($\tau_{\rm disk} \lesssim 5$ Myr, Hernández et al. 2008).
- As the star evolves, a radiative core forms during the pre-main sequence within an initially fully convective structure, and subsequently evolves into the fully developed radiative interior region around the ZAMS epoch; changes in the stellar radius, the relative size and mass of the radiative zone and convective envelope, and their moments of inertia are taken into account, based on non-rotational stellar evolution tracks (see below for details).
- The magnetized stellar wind effectively applies a braking torque at the surface (e.g., Schatzman 1962; Kraft 1967; Skumanich 1972), removing angular momentum from the convective envelope at the rate $\frac{dJ}{dt}\big|_{\rm wb}$; the choice of this "wind braking law", which is one of the largest sources of uncertainty in our model, is further discussed below.
- As the convective envelope loses angular momentum through the magnetized wind, an angular momentum excess develops between the radiative interior and the convective envelope; this excess is redistributed over time, as evidenced by the almost uniform solar rotation profile (Schou et al. 1998), but this process is still not well understood, so we model it parametrically by introducing a rotational coupling timescale $\tau_{\rm cpl}$.

Mathematically, the model consists of two coupled ordinary differential equations for the evolution of Ω_c and Ω_e:

$$
\begin{aligned}
&t \le \tau_{\rm disk}: \\
&I_c \frac{{\rm d}\Omega_c}{{\rm d}t} = +\frac{2}{3}\frac{{\rm d}M_c}{{\rm d}t} R_c^2\,\Omega_e - \frac{\Delta J}{\tau_{\rm cpl}} - \frac{{\rm d}I_c}{{\rm d}t}\Omega_c; \\
&\frac{{\rm d}\Omega_e}{{\rm d}t} = 0; \\
&t > \tau_{\rm disk}: \\
&I_c \frac{{\rm d}\Omega_c}{{\rm d}t} = +\frac{2}{3}\frac{{\rm d}M_c}{{\rm d}t} R_c^2\,\Omega_e - \frac{\Delta J}{\tau_{\rm cpl}} - \frac{{\rm d}I_c}{{\rm d}t}\Omega_c; \\
&I_e \frac{{\rm d}\Omega_e}{{\rm d}t} = -\frac{2}{3}\frac{{\rm d}M_c}{{\rm d}t} R_c^2\,\Omega_e + \frac{\Delta J}{\tau_{\rm cpl}} - \frac{{\rm d}I_e}{{\rm d}t}\Omega_e + \frac{{\rm d}J}{{\rm d}t}\Big|_{\rm wb},
\end{aligned}
\tag{1}
$$

where M_c, R_c, I_c are the mass, radius, and moment of inertia of the radiative interior, I_e is the moment of inertia of the convective envelope, and $\Delta J = \frac{I_c I_e}{I_c + I_e}(\Omega_c - \Omega_e)$ (cf. MacGregor & Brenner 1991).

The equations are integrated using the ODE solver `solve_ivp`, which is part of the `scipy.integrate` package. We selected the integration method RK45, an embedded explicit Runge-Kutta method of order 5(4). During the course of the integration, the stellar structure parameters are obtained by interpolation from stellar evolutionary tracks, using `splrep` with pre-built spline fits constructed with `BSpline`, both part of `scipy.interpolate`. The evolutionary tracks were constructed with solar metallicity and mass in the range $0.4-1.25\,M_\odot$ in steps of $0.05\,M_\odot$ using the Yale Rotational stellar Evolution Code (YREC) in its non-rotational configuration (Demarque et al. 2008).

Our wind braking law follows the classic structure:

$$
\frac{{\rm d}J}{{\rm d}t}\Big|_{\rm wb} = -K_w \cdot f_{M_*} \cdot \left(\frac{\Omega_e}{\Omega_\odot}\right)^3, \tag{2}
$$

where K_w is a scaling constant (in the following, numerical values of K_w are quoted in units of $1.13 \cdot 10^{47}$ g cm^2 s for convenience, cf. Kawaler 1988). The Ω_e^3 dependence is based on theoretical and empirical estimates of the scaling of the surface magnetic field with surface rotation ("dynamo law"; e.g., Stix 1972;

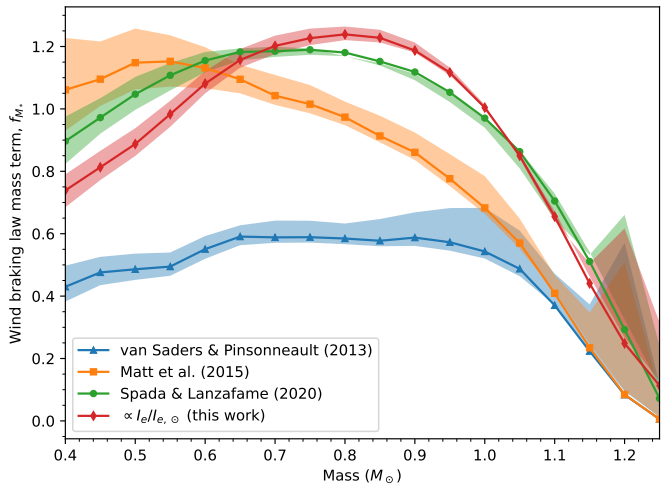

Fig. 3. Prescriptions for mass dependence of wind braking law, f_{M_*}, considered in our models. The range of variability due to stellar evolution in the age range spanned by our models (≈0.1−4 Gyr) is also shown. The increase in the variability width at the two ends of the mass range is due to the prolonged pre-main sequence phase, and to the earlier onset of the post-main sequence phase, respectively, in comparison with the stars in the middle of the mass range.

Linsky & Saar 1987; Kawaler 1988), leading to a rotational evolution approximately following the $P_{\rm rot} \propto t^{1/2}$ Skumanich law (Skumanich 1972). We do not attempt to introduce any saturation effect of the dynamo law, since the present work focuses on the evolution of the slow–rotator sequence, which is composed of stars in the non-saturated regime (by definition).

The term f_{M_*}, on the other hand, imparts a mass dependence to the wind braking law by specifying an explicit dependence on selected stellar structure quantities (note that in this way an additional indirect, mostly negligible, time dependence, due to the evolution of the stellar parameters, is also introduced). This term is crucial to model satisfactorily the slow–rotator sequence (see Barnes & Kim 2010, LS15; SL20 for details).

Several f_{M_*} prescriptions exist in the literature whose motivations range from purely theoretical models, to fits of theoretical models, to semi-empirical, to purely empirical considerations. In this work, we discuss models implementing the following mass dependence terms of the wind braking law:

$$f_{M_*} = \left(\frac{R_*}{R_\odot}\right)^{3.1} \left(\frac{M_*}{M_\odot}\right)^{-0.22} \left(\frac{L_*}{L_\odot}\right)^{0.56} \left(\frac{P_s}{P_{s,\odot}}\right)^{0.44} \left(\frac{\tau_c}{\tau_{c,\odot}}\right)^2 ; \quad (3)$$

$$f_{M_*} = \left(\frac{R_*}{R_\odot}\right)^{3.1} \left(\frac{M_*}{M_\odot}\right)^{0.5} \left(\frac{\tau_c}{\tau_{c,\odot}}\right)^2 ; \quad (4)$$

$$f_{M_*} = \left(\frac{I_*}{I_\odot}\right)\left(\frac{\tau_c}{\tau_{c,\odot}}\right); \quad (5)$$

$$f_{M_*} = \left(\frac{I_e}{I_{e,\odot}}\right). \quad (6)$$

In the equations above, L_* and P_s are the luminosity and the photospheric pressure of the star, respectively; τ_c is the global convective turnover timescale[1]; $I_* = I_e + I_c$ is the moment of inertia of the whole star. Each of these quantities enters f_{M_*} scaled over its respective solar counterpart, which is indicated with the additional subscript "⊙". During the integration of equations (1), the dependence on these additional structure quantities is handled in the same way as discussed above for the rotation-related parameters.

Detailed discussions of equations (3)–(5) can be found in Matt et al. (2012) and van Saders & Pinsonneault (2013), Matt et al. (2015), and SL20, respectively. Equation (6) is original to the present work and will be discussed further below.

The functional dependence of f_{M_*} on the mass of the star according to equations (3)–(6) is illustrated in Figure 3, which also shows the range of variation due to stellar evolution between 0.1 and 4.0 Gyr. It is clear from the figure that the indirect time dependence introduced by stellar evolution is quite modest, except at the two extremes of the mass range. The widening of the f_{M_*} time variation at $M_* \lesssim 0.5\,M_\odot$ and at $M_* \gtrsim 1.15\,M_\odot$ is due to the non-negligible overlap of the pre-main sequence and of the post-main sequence phases, respectively, with the age range considered here.

The following quantities are treated as adjustable parameters in our rotational evolution model:

- The initial rotation period P_0;
- The circumstellar disk lifetime $\tau_{\rm disk}$;
- The scaling constant K_w in the wind braking law;
- The rotational coupling timescale $\tau_{\rm cpl}$.

The effect of the parameters P_0 and $\tau_{\rm disk}$ is mostly limited to the very early stages of the rotational evolution, which should be practically forgotten as soon as stars settle on the slow–rotator sequence. We thus treat P_0 and $\tau_{\rm disk}$ as nuisance parameters, which we fit independently of stellar mass. In contrast, based on the results of LS15; SL20, we anticipate that significantly mass-dependent K_w and $\tau_{\rm cpl}$ will be required to reproduce the observations, for different reasons. The dependence of K_w on stellar mass can be considered as an empirical correction to the shortcomings of the assumed f_{M_*} prescription. A mass-dependent $\tau_{\rm cpl}$, on the other hand, is critical to properly model the stalled magnetic braking phase.

3.3. Fitting the parameters of the two-zone model

Once the stellar evolution tracks and the input parameters are specified, our rotational evolution model of the slow–rotator sequence is completely determined. We can thus construct snapshots of the sequence at the nominal ages of the open clusters in our catalog (see Table 1). In practice, we do so by calculating the rotational evolution of stars in the mass range 0.4−1.25 $M_\odot$, in steps of 0.05 $M_\odot$, independently for each mass; as a result, our calculated slow–rotator sequence is sampled at 18 points equally spaced in mass.

Each of the modeled sequence snapshots is compared with its empirical counterpart of the same age, obtained from the non-parametric fits described in Section 3.1. In this way, we form the residuals, in the sense of observed-minus-calculated (O–C) differences, normalized to the standard deviations of the non-parametric fits. Our goodness-of-fit metric is defined as a standard chi-square in terms of these residuals:

$$\chi^2 = \sum_{i=1}^{N} \frac{(O_i - C_i)^2}{\sigma_i^2}, \quad (7)$$

where the index i runs over the sampled masses in the sequence and, in turn, over the ages of the clusters in our catalog. It should be noted that the empirical slow–rotator sequence does not exist

[1] The "global" (or "nonlocal") convective turnover timescale is calculated as the integral of the reciprocal of the local convective velocity, v_c, extended from the bottom of the convection zone to the surface: $\tau_c = \int_{R_c}^{R_*} \frac{{\rm d}r}{v_c}$ (Kim & Demarque 1996).

Table 2. Summary of best-fitting parameters in our rotational evolution models (see text for details).

Model	P_0 (days)	$\tau_{\rm disk}$ (Myr)	f_{M_*}	χ^2	χ^2_ν
vs13	7.04	4.54	Eq. (3)	152.6	2.01
ma15	4.01	3.07	Eq. (4)	141.3	1.86
sl20	7.72	4.82	Eq. (5)	120.7	1.59
ienv	7.18	4.80	Eq. (6)	108.2	1.42
bpl	10.1	4.57	1.0	97.7	1.04

in the full mass range at all ages, due both to incomplete data coverage and to the mass-dependence of the timescale of convergence on the sequence (i.e., lower mass stars converge to the sequence at later ages than their more massive counterparts). As a result, the total number of empirical constraints on the fit is $N = 114$, out of the maximum possible values of 144 (=18 masses ×8 clusters).

We determine the best-fitting values of the parameters using a standard least-squares approach, as implemented in the `least_squares` function of the `scipy.optimize` package. As explained above, while the parameters P_0 and $\tau_{\rm disk}$ are assumed to be independent of the mass, the parameters K_w and $\tau_{\rm cpl}$ are allowed to take different values for each stellar mass. The total number of free parameters in our fits is therefore $p = 2+2\times18 = 38$, independent of the prescription chosen for $f(M_*)$.

4. Results

We fitted our rotational evolution models to the empirical constraints on the slow–rotator sequence discussed in Section 3.1, using the least-squares procedure described in Section 3.3. The results of these fits are summarized in Table 2. The first four entries in the Table, models "vs13", "ma15", "sl20", and "ienv", differ in the mass dependence of the wind braking law, f_{M_*}, while model "bpl" is qualitatively different and will be discussed in detail in Section 4.2. The reduced chi-square is $\chi^2_\nu = \chi^2/(N-p)$, where N and p are the number of constraints and free parameters in the fit for each model, respectively.

In addition to the chi-square and the reduced chi-square values, Table 2 lists the best-fitting P_0 and $\tau_{\rm disk}$ for each model. The mass-dependent best-fitting K_w and $\tau_{\rm cpl}$ are discussed in detail in the next two sections. To illustrate our results, we plot the rotational isochrones for model "ienv" ($f_{M_*} = I_e/I_{e,\odot}$), together with the individual data and the non-parametric fit of the slow–rotator sequence in Figure 4. The rotational evolution of individual stars in our mass range according to the same model is plotted in Figure 5.

Comparing the chi-square values in Table 2, we see that the most satisfactory fit is obtained with $f_{M_*} = I_e/I_{e,\odot}$, equation (6). We propose this novel form of f_{M_*} mostly on empirical grounds. We note (see Figure 3) the overall similarity of the mass dependence introduced by equations (5) and (6), the latter being a modification suggested by LS15 of an earlier form, proposed in turn by Barnes & Kim (2010). An independent argument in support of equation (6) is offered in Section 4.2.

4.1. The rotational coupling timescale

The best-fitting values of the rotational coupling timescale $\tau_{\rm cpl}$ turn out to be fairly insensitive to the choice of f_{M_*} (see Figure 6). This is in itself an important result, because a strong correlation between the wind braking term and the angular momentum redistribution term in equations (1) could not have been ruled out a priori.

Notably, the largest differences among the $\tau_{\rm cpl}$ fitted with different f_{M_*} terms are confined to $M_* \gtrsim 1.1\,M_\odot$. In this mass subrange, the best-fitting $\tau_{\rm cpl}$ exhibits relatively large, non-smooth fluctuations. A similar situation, albeit characterized by more modest amplitudes, also arises for $M_* \approx 0.4\,M_\odot$. In general, we can expect our fits to be the least robust at the two ends of the mass range, since in those regimes (i) the empirical constraints on the slow–rotator sequence are often missing in the color–period diagrams of the clusters in our catalog; (ii) the largest variations of the stellar parameters due to stellar evolution occur. Indeed, we observe a similar effect in the K_w best-fitting values (see Figure 7).

When the coupling timescale is sufficiently short, the star rotates essentially as a solid body throughout most of its evolution. In this regime, the rotational evolution model becomes increasingly insensitive to the precise value of $\tau_{\rm cpl}$. Best-fitting values of $\tau_{\rm cpl} \lesssim 10$ Myr are therefore intrinsically poorly constrained, which explains, at least in part, the large relative variations obtained for $M_* \gtrsim 1.1\,M_\odot$.

For these reasons, it is meaningful and practically advantageous to extract the general behavior of $\tau_{\rm cpl}$, while filtering out the noisy fluctuations at the high end of the mass range. For this purpose we represent the mass dependence of the rotational coupling timescale obtained from our fits with a broken power law of the form:

$$\tau_{\rm cpl} = \tau_0 \begin{cases} \left(\frac{M_*}{M_b}\right)^{-\alpha_1}, & M_* < M_b \\ \left(\frac{M_*}{M_b}\right)^{-\alpha_2}, & M_* > M_b. \end{cases} \quad (8)$$

By visual inspection, we set the mass at which the exponent break occurs to $M_b = 0.60\,M_\odot$, and we derive the parameters τ_0, α_1, and α_2 from a standard curve fit performed with `scipy.optimize.curve_fit`. We obtain:

$$\tau_0 = 565. \pm 15.\,\text{Myr}; \quad \alpha_1 = 1.83 \pm 0.09; \quad \alpha_2 = 5.72 \pm 0.32. \quad (9)$$

The resulting curve, plotted in Figure 6 as a dashed black line, provides a very good parametric representation of our empirically derived mass dependence of the rotational coupling timescale. For reference, this parametrization corresponds to $\tau_{\rm cpl} = 30.4 \pm 5.0$ Myr for a $1.0\,M_\odot$ star. Along with the higher mass regime exponent α_2, this value can be directly compared with the best-fitting values in the power law function proposed by SL20: $\tau^{\rm SL20}_{\rm cpl,\odot} = 22$ Myr, $\alpha^{\rm SL20} = 5.6$.

Our current broken power law model of $\tau_{\rm cpl}$ thus extends our previous results, while being completely consistent with it within their common range of applicability (although the SL20 power law parameters were presented without formal error bars, it is reasonable to assume that their uncertainties should be comparable to those of our current broken power law fit). The agreement of our present and past results is encouraging, also considering that the power law behavior of $\tau_{\rm cpl}$ found by LS15 has been confirmed, both qualitatively and quantitatively, by a completely independent study (Somers & Pinsonneault 2016).

Using the broken power law parametrization for the rotational coupling timescale not only filters out the large relative fluctuations of $\tau_{\rm cpl}$ at the high mass end of the range, but can also reduce the total number of free parameters in the least-squares fit. The corresponding model is referred to as "bpl" in Table 2 and is discussed in the following (see the next section for details).

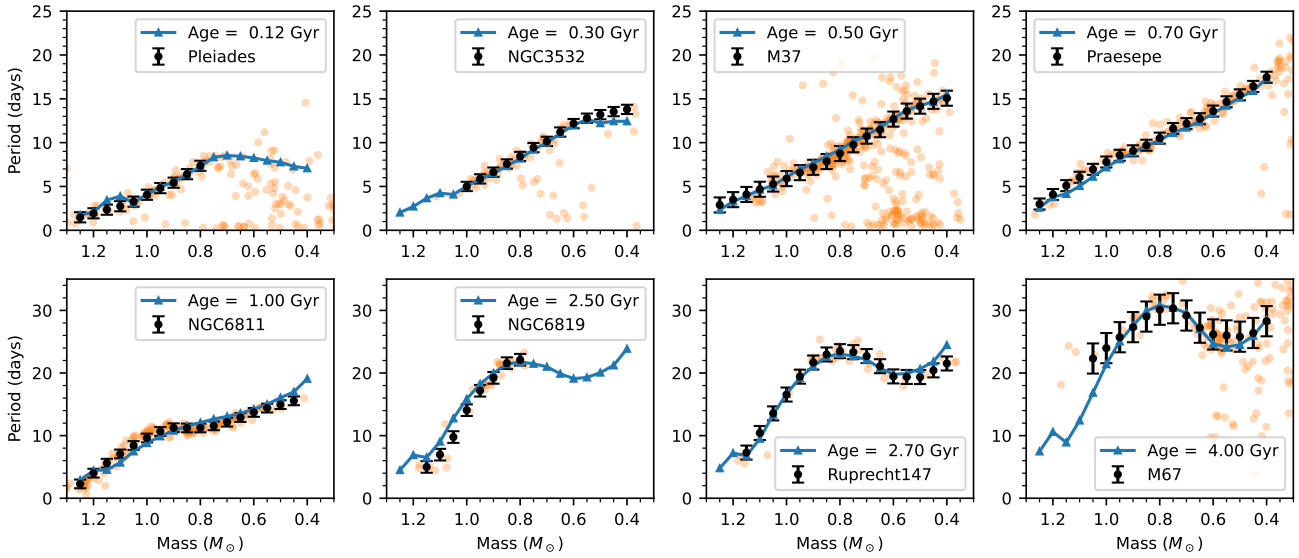

Fig. 4. Rotational isochrones from our model "ienv" (blue lines with triangles) compared with non-parametric fit of slow–rotator sequence (black circles with error bars) in mass–period diagram of clusters in our compilation. Individual stars are also shown as orange circles.

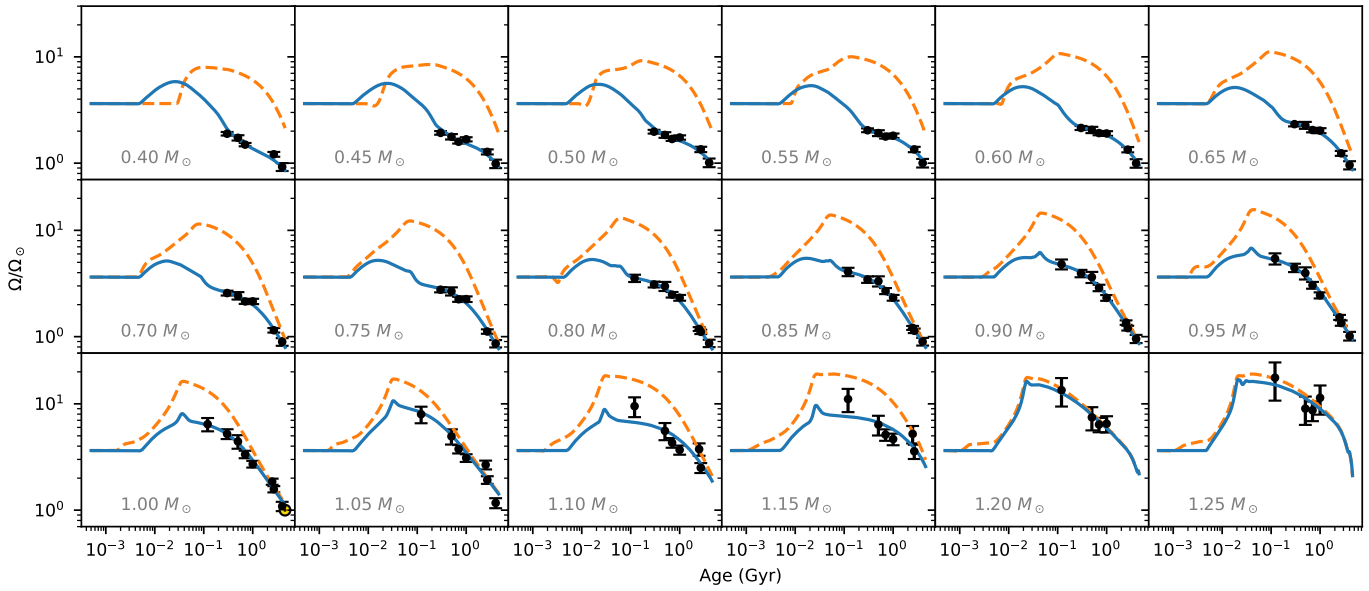

Fig. 5. Rotational evolution according to model "ienv" for stars of mass 0.4–1.25 $M_\odot$. In each panel, the angular velocity of the convective envelope is plotted as a blue solid line, the angular velocity of the radiative interior is plotted as a dashed orange line, and the constraints from the non-parametric fits of the slow–rotator sequence are shown as black circles with error bars (the surface period of the Sun is also shown in the appropriate panel).

4.2. The wind braking law mass dependence

Figure 7 compares the best-fitting K_w's obtained for each stellar mass with different choices of the mass dependence term f_{M_*}, as reported in Table 2. Ideally, the term f_{M_*} should fully account for the mass dependence of the wind braking law, resulting in optimized K_w nearly independent of mass. In other words, the smallness of the mass dependence found in the fitted K_w can be taken as a measure of the quality of the f_{M_*} prescription used (cf., the discussion in LS15). We see from Figure 7 that models "sl20" and "ienv" are the best performing with respect to this criterion.

To take advantage of the regularized empirical mass dependence of $\tau_{\rm cpl}$ as a broken power law expressed by equation (8) (see Section 4.1), we have performed an additional fit, which we refer to as model "bpl" in the following. This fit is qualitatively different from the others in two respects:

1. The rotational coupling timescale is not freely adjusted, but prescribed according to equations (8) with the coefficients (9);
2. We set $f_{M_*} = 1$, so that the mass dependence of the wind braking law is fully encoded in the adjusted K_w's.

Figure 8 shows the fit corresponding to model "bpl" along with the ones based on the f_{M_*} prescriptions in equations (3)–(6)

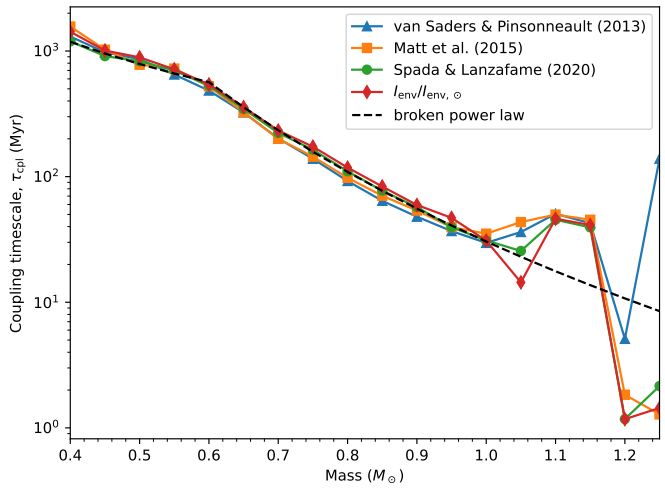

Fig. 6. Best-fitting τ_{cpl} resulting from least-squares optimization procedure described in Section 3.3. The dashed black line represents a best-fit of the common τ_{cpl} behavior with a broken power law (see equation 8 and the discussion in the text).

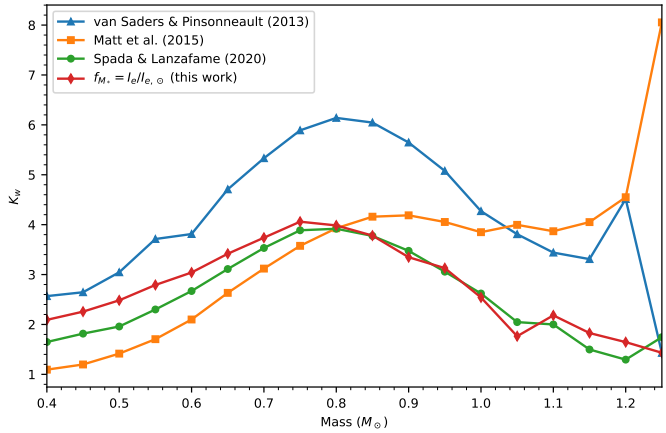

Fig. 7. Best-fitting K_w resulting from least-squares optimization procedure described in Section 3.3.

(dashed black line with open circles; cf., the corresponding entry in Table 2). In order to make the comparison in Figure 8 meaningful, in this case the product $K_w \times f_{M_*}$ is plotted for each model.

Because τ_{cpl} is held fixed, model "bpl" contains $p = 2 + 18 = 20$ adjustable parameters (i.e., P_0, τ_{disk}, and the 18 mass-dependent K_w values). This is therefore the most economical of our models and thus the closest to extracting an empirical $K_w \times f_{M_*}$ from our data sample. Of course, even in this case, the fitted mass dependence cannot be considered, sensu stricto, fully empirical, since the fitting procedure introduces some model-dependent assumptions. Another advantage of the approach in model "bpl" is that the fluctuations of τ_{cpl} at the two extremes of the mass range are effectively removed.

The "semi-empirical" fit of $K_w \times f_{M_*}$ obtained with model "bpl" is therefore a valuable reference for comparison and a useful guide to formulate a wind braking law with an improved mass dependence term. In particular, since, as stated above, the ideal mass term $\tilde{f}_{M_*}$ should be the one for which the corresponding best-fitting $\tilde{K}_w$ is independent of the stellar mass, we can speculate that:

$$\left.\begin{array}{l}(\tilde{K}_w \times \tilde{f}_{M_*}) = (K_w^{\rm bpl} \times 1);\\ \tilde{K}_w \approx \text{const.}\end{array}\right\} \Rightarrow \tilde{f}_{M_*} \propto K_w^{\rm bpl},$$

where $K_w^{\rm bpl}(M_*)$ are the best-fitting values of the wind braking law constant from the fit of model "bpl".

In other words, the quantities $K_w^{\rm bpl}(M_*)$ can be used to constrain the optimal mass dependence of f_{M_*} within an overall multiplicative constant. As a step in this direction, we note that our model "ienv" results in a $K_w \times f_{M_*}$, which traces most closely the semi-empirical one, the difference between the two being at most 20% between 0.4 and 1.1 $M_\odot$.

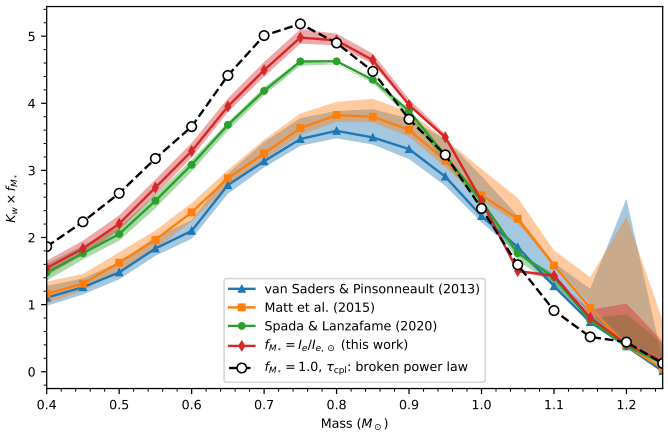

Fig. 8. Similar to Figure 7, but showing product $K_w \times f_{M_*}$, and including fit obtained with model "bpl". Note the very close agreement between the latter and model "ienv".

4.3. A posteriori validation

The catalog of rotation period measurement recently assembled by Van-Lane et al. (2025) in support of their `ChronoFlow` gyrochronology model provides the opportunity for independent validation of our work. Indeed, our literature compilation, including the selection of open clusters, choice of fiducial ages, sources of rotation periods, Gaia colors, cluster membership information, detailed in Section 2, is completely independent of theirs. In addition, since the `ChronoFlow` catalog features a more extensive compilation of open clusters than ours, we can use it to test our rotational models on data which were not included in the fitting procedure.

The comparison is summarized in the plots in Figure 9. In this figure, the data from the `ChronoFlow` catalog are plotted in blue, while the data from our catalog, where available, are shown in orange; rotational isochrones from our model "ienv" are plotted as solid black lines with triangles. For internal consistency of the comparison, the isochrones shown in each panel of Figure 9 are calculated at the fiducial ages of the clusters adopted in the `ChronoFlow` catalog, which differ from our nominal ages (Table 1) as follows: Pleiades: 100 vs 120 Myr; NGC 3532: 400 vs 300 Myr; M37: 450 vs 500 Myr; Praesepe: 720 vs 700 Myr; NGC 6819: 2.31 vs 2.5 Gyr; Ruprecht 147: 2.45 vs 2.7 Gyr; M67: 3.87 vs 4.0 Gyr. This comparison thus seems to indicate that moderate changes in the nominal ages do not significantly affect the final results.

The agreement of the model with the data, in particular with the slow–rotator sequence or at least the upper envelope

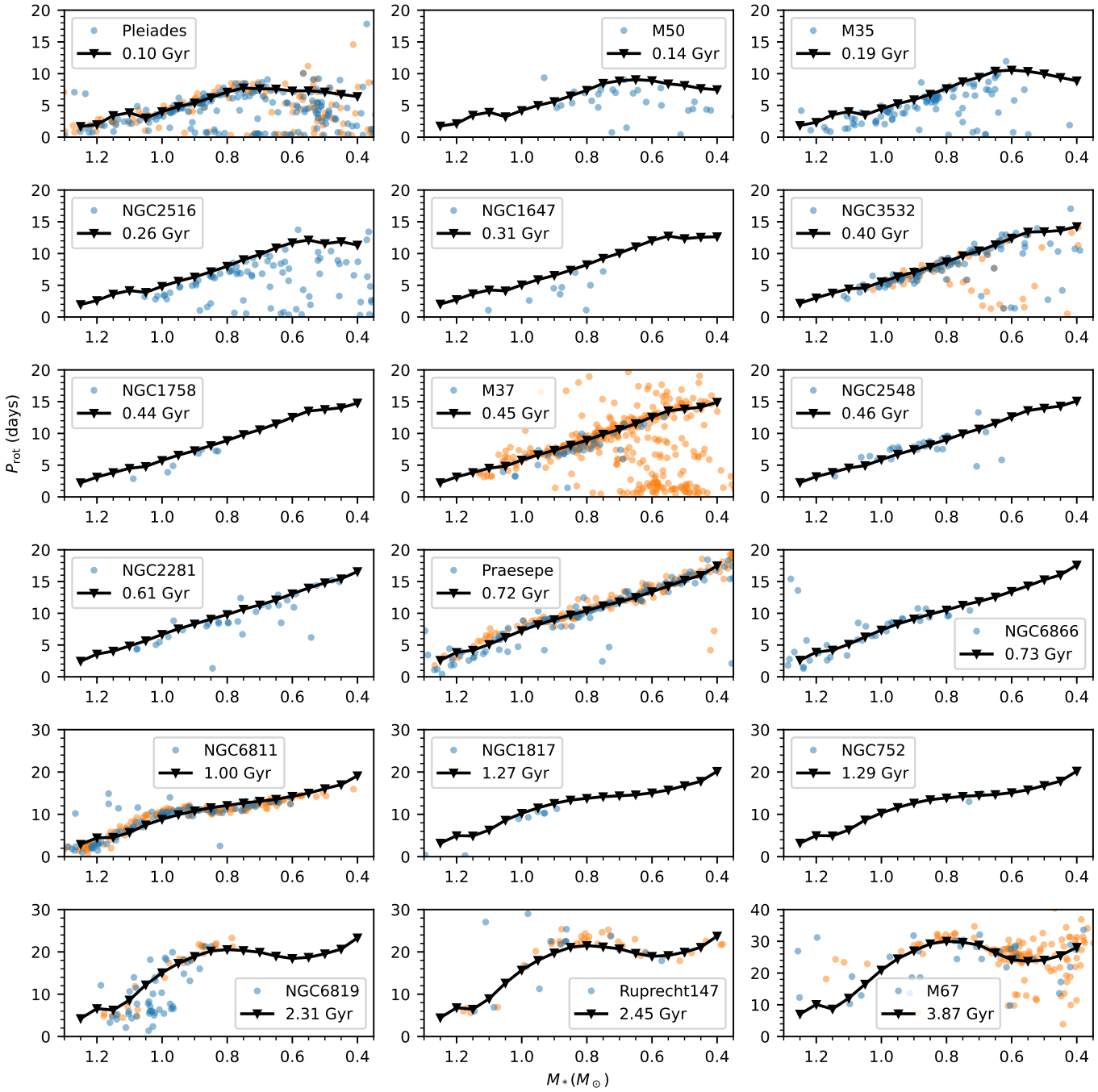

Fig. 9. Comparison between `ChronoFlow` catalog (Van-Lane et al. 2025, blue), our data compilation (orange), and our best model, using f_{M_*} in equation (6) (black triangles with solid lines). Note that the rotational isochrones shown are calculated at the fiducial ages of the `ChronoFlow` catalog, which are different from ours for some clusters (see text for details).

of the rotation period distribution of each cluster, is very good. This comparison strengthens our confidence in our modeling approach and, in particular, in our new proposal for the wind mass dependence prescription, $f_{M_*} \propto I_e$.

5. Discussion

In this paper, we adopted a modeling framework for the rotational evolution of solar-like stars which is capable of reproducing the evolution of the slow–rotator sequence as observed in Galactic open clusters. With the present revision of the modeling parameters, our models are applicable in the entire mass range encompassing stars with solar-like interior structure (i.e., a radiative interior and a convective envelope) during their main sequence phase, namely, 0.4–1.25 $M_\odot$. Our models reproduce satisfactorily the evolution of the slow–rotator sequence in the age interval from ≈100 Myr to 4 Gyr.

A key feature of our models is that they account for the differential rotation between the radiative interior and the convective envelope, which develops as the angular momentum redistribution from the interior lags behind the loss at the surface via magnetic braking. The temporary rotational decoupling,

and subsequent recoupling, is indeed considered the leading explanation for the observed non-monotonic rotational evolution, or stalled braking, first observed between the Praesepe and NGC 6811 clusters, i.e., between 0.7 and 1.0 Gyr, for stars of approximately 0.8 $M_\odot$ (Curtis et al. 2019, 2020; Angus et al. 2020; Gordon et al. 2021; Santos et al. 2025).

The rotational coupling timescale $\tau_{\rm cpl}$, which parametrizes the angular momentum transport efficiency in our models, was found by LS15 and SL20 to be strongly mass-dependent, following a power law with negative exponent. This result is confirmed by our present fit, and the revised coefficients are in good agreement with those found in our previous work.

It was further pointed out by SL20 that, as a consequence of the mass dependence of $\tau_{\rm cpl}$, stars of progressively lower mass should experience stalling of their rotational braking at increasingly later ages, since the longer $\tau_{\rm cpl}$ (see Figure 6) results in progressively later recoupling. This prediction appears to be confirmed by the most recent observations. In clusters of age $\gtrsim$2 Gyr, the empirical slow–rotator sequence features a characteristic dip at masses below 0.8 $M_\odot$. The minimum of this dip shifts to a lower mass as the age of the cluster increases, as can be seen from the comparison of NGC 6811, Ruprecht 147, and M67 (cf. Figure 4). This feature is recovered by our models, and we speculate that it is the signature of stalled braking occurring at increasingly lower masses as a consequence of the mass-dependence of $\tau_{\rm cpl}$. This "stalling wave" was predicted by SL20, and is reproduced by our current models.

Our results provide semi-empirical constraints on the mass dependence of the two key processes driving the rotational evolution of solar-like stars: the angular momentum transport in the interior and the wind braking at the surface (see Sections 4.1 and 4.2). While this scaling may be of interest in exploring candidate mechanisms for angular momentum transport in stellar radiative interiors (e.g., Fuller et al. 2014; Eggenberger et al. 2022; Meduri et al. 2024), we emphasize that our results do not identify the underlying physical process and should not be interpreted as providing a complete theoretical explanation. Similarly, the empirical $K_w \times f_{M_*}$ relation can serve as a practical guide for calibrating MHD wind models as a function of mass.

From a practical perspective, our models represent a step toward a physics-informed gyrochronology relation, complementing purely empirical or data-driven approaches (e.g., Barnes 2010; Van-Lane et al. 2025).

Because our models adopt the two-zone framework, their extension to stars without a solar-like internal structure (most notably, fully convective stars, $M_* \lesssim 0.35\,M_\odot$) is not straightforward. In this regime, the physical assumptions underlying the core-envelope decoupling formalism are no longer valid. In this context, recent work by Chiti et al. (2024) indicates that rotation periods increase sharply across a narrow effective temperature interval near the fully convective boundary. This behavior may reflect the structural changes (e.g., convection zone depth, convective turnover timescale) associated with the transition and its dependence on mass, metallicity, and age, potentially linked to the ^{3}He-burning instability discovered by van Saders & Pinsonneault (2012). Clearly, models based on different assumptions and likely belonging to a different model class are required to incorporate the fully convective regime within a unified framework for solar-like and low-mass stellar rotational evolution (see also Lu et al. 2024).

The present study focuses on the Skumanich-like regime of rotational evolution, in which spin down by magnetic wind braking continues indefinitely. This framework has proven robust up to about solar age, and it remains the natural reference against which new developments are measured. Currently, the 4 Gyr-old open cluster M67 provides the oldest available rotational constraints, and its stellar population is consistent with traditional spin-down laws at least up to that age.

Recent observations of field stars suggest a departure from standard magnetic braking behavior, with evidence for an abrupt reduction of wind torque as the Rossby number (the ratio between the rotation period and the convective turnover timescale) approaches a critical value (van Saders et al. 2016; Metcalfe et al. 2025). Because the relevant control parameter is the Rossby number, the age at which weakened magnetic braking sets in is intrinsically mass-dependent. It cannot therefore be ruled out that some of the most massive stars in the open clusters considered here may already be in this regime. In this work, however, we do not attempt a quantitative assessment, in part owing to the multiple, non-equivalent definitions of the Rossby number used across theoretical and observational studies.

Although our models do not attempt to capture the weakened magnetic braking regime, they provide a controlled baseline that can be extended once the relevant physical processes (such as changes in coronal magnetic topology, dynamo action, or the coupling between the stellar interior and wind) are better understood. Future work may therefore build upon the present results by introducing prescriptions for weakened braking at the critical Rossby number, guided by asteroseismic and Gaia-based constraints. In this way, the applicability of our approach could be extended from the well-calibrated young and middle-aged populations to encompass the full main-sequence lifetime of solar-like stars, and possibly beyond.

6. Conclusions

The present paper extends and complements the results of our previous work, by bringing to fruition the latest observational constraints recently obtained through ground- and space-based photometric surveys of stellar rotation.

Our improved models can satisfactorily reproduce the observed evolution of the slow–rotator sequence in open clusters from 100 Myr to 4 Gyr for the entire range of solar-like stars (0.4−1.25 $M_\odot$). Our physically motivated parametric model can constrain the dependence on stellar mass of the two key processes that drive the rotational evolution of solar-like stars, namely, the wind braking at the surface and the angular momentum transport in the interior.

We find that the rotational coupling timescale as a function of stellar mass follows very closely a broken power law relation, with the exponent change occurring at 0.6 $M_\odot$, i.e., at the transition from late to early K-type stars. Importantly, the rotational coupling timescale as a function of stellar mass follows this broken power law relation independently of the choice of the wind braking law, demonstrating that the coupling mass dependence is robust to variations in surface torque prescriptions. The optimized parameters of the broken power law are in very good agreement with our previous findings, which have also been independently confirmed by other authors.

By setting the rotational coupling timescale according to the optimized broken power law, we can reduce the number of adjustable parameters in the rotational evolution model and derive a "semi-empirical" mass dependence of the wind braking law, i.e., one obtained with a minimum of model-dependent assumptions.

Finally, we propose a novel formulation for the mass dependence of the wind braking law, proportional to the moment of inertia of the convective envelope of the star. Such formulation

results in the best agreement with the observations among the functional wind braking laws we tested, and is indirectly supported by its close resemblance with the semi-empirical mass scaling.

Acknowledgements. This research has made use of the following software: NumPy (Harris et al. 2020), SciPy (Virtanen et al. 2020), Matplotlib (Hunter 2007). FS is funded by the European Union – NextGenerationEU RRF M4C2 1.1 No.2022HY2NSX, "CHRONOS: adjusting the clock(s) to unveil the CHRONO-chemo-dynamical Structure of the Galaxy" (PI: S. Cassisi). FS gratefully acknowledges the inspiring mentorship and personal kindness of the late Pierre Demarque, and the friendship and professional support of the late Patrick Gaulme, both extended over many years of close scientific collaboration.

References

Aerts, C., Mathis, S., & Rogers, T. M. 2019, ARA&A, 57, 35
Amard, L., & Matt, S. P. 2020, ApJ, 889, 108
Andrae, R., Fouesneau, M., Sordo, R., et al. 2023, A&A, 674, A27
Angus, R., Beane, A., Price-Whelan, A. M., et al. 2020, AJ, 160, 90
Barnes, S. A. 2003, ApJ, 586, 464
Barnes, S. A. 2010, ApJ, 722, 222
Barnes, S. A., & Kim, Y.-C. 2010, ApJ, 721, 675
Barnes, S. A., Spada, F., & Weingrill, J. 2016, Astron. Nachr., 337, 810
Bragaglia, A., Carretta, E., Gratton, R. G., et al. 2001, AJ, 121, 327
Brown, T. M. 2014, ApJ, 789, 101
Cantiello, M., Mankovich, C., Bildsten, L., et al. 2014, ApJ, 788, 93
Charbonneau, P., & MacGregor, K. B. 1993, ApJ, 417, 762
Charbonnel, C., & Talon, S. 2005, Science, 309, 2189
Chiti, F., van Saders, J. L., Heintz, T. M., et al. 2024, ApJ, 977, 15
Choi, J., Dotter, A., Conroy, C., et al. 2016, ApJ, 823, 102
Christensen-Dalsgaard, J., & Schou, J. 1988, Seismology of the Sun and Sun-Like Stars, 286, 149
Cleveland, W. S., Grosse, E., & Shyu, W. M. 2017, Local Regression Models. Statistical models in S, 309
Curtis, J. L., Agüeros, M. A., Douglas, S. T., et al. 2019, ApJ, 879, 49
Curtis, J. L., Agüeros, M. A., Matt, S. P., et al. 2020, ApJ, 904, 140
De Angeli, F., Weiler, M., Montegriffo, P., et al. 2023, A&A, 674, A2
Deheuvels, S., Doğan, G., Goupil, M. J., et al. 2014, A&A, 564, A27
Deheuvels, S., Ballot, J., Eggenberger, P., et al. 2020, A&A, 641, A117
Demarque, P. R., & Larson, R. B. 1964, ApJ, 140, 544
Demarque, P., Guenther, D. B., Li, L. H., et al. 2008, Ap&SS, 316, 31
Dungee, R., van Saders, J., Gaidos, E., et al. 2022, ApJ, 938, 118
Eggenberger, P., Maeder, A., & Meynet, G. 2005, A&A, 440, L9
Eggenberger, P., Deheuvels, S., Miglio, A., et al. 2019, A&A, 621, A66
Eggenberger, P., Moyano, F. D., & den Hartogh, J. W. 2022, A&A, 664, L16
Fritzewski, D. J., Barnes, S. A., James, D. J., et al. 2021, A&A, 652, A60
Fuller, J., Lecoanet, D., Cantiello, M., et al. 2014, ApJ, 796, 17
Gaia Collaboration (Babusiaux, C., et al.) 2018, A&A, 616, A10
Gallet, F., & Bouvier, J. 2013, A&A, 556, A36
Gallet, F., & Bouvier, J. 2015, A&A, 577, A98
Garraffo, C., Drake, J. J., Dotter, A., et al. 2018, ApJ, 862, 90
Godoy-Rivera, D., Pinsonneault, M. H., & Rebull, L. M. 2021, ApJS, 257, 46
Gordon, T. A., Davenport, J. R. A., Angus, R., et al. 2021, ApJ, 913, 70
Gruner, D., Barnes, S. A., & Weingrill, J. 2023, A&A, 672, A159
Harris, C. R., Millman, K. J., van der Walt, S. J., et al. 2020, Nature, 585, 357
Hartman, J. D., Gaudi, B. S., Pinsonneault, M. H., et al. 2009, ApJ, 691, 342
Hernández, J., Hartmann, L., Calvet, N., et al. 2008, ApJ, 686, 1195
Hunter, J. D. 2007, Comput. Sci. Eng., 9, 90
Kawaler, S. D. 1988, ApJ, 333, 236
Kim, Y.-C., & Demarque, P. 1996, ApJ, 457, 340
Koenigl, A. 1991, ApJ, 370, L39
Kraft, R. P. 1967, ApJ, 150, 551
Krishnamurthi, A., Pinsonneault, M. H., Barnes, S., et al. 1997, ApJ, 480, 303
Lanzafame, A. C., & Spada, F. 2015, A&A, 584, A30
Lanzafame, A. C., Distefano, E., Barnes, S. A., et al. 2019, ApJ, 877, 157
Linsky, J. L., & Saar, S. H. 1987, Lect. Notes Phys., 291, 44
Lu, Y. L., See, V., Amard, L., et al. 2024, Nat. Astron., 8, 223
MacGregor, K. B., & Brenner, M. 1991, ApJ, 376, 204
Matt, S. P., MacGregor, K. B., Pinsonneault, M. H., et al. 2012, ApJ, 754, L26
Matt, S. P., Brun, A. S., Baraffe, I., et al. 2015, ApJ, 799, L23
Meduri, D. G., Jouve, L., & Lignières, F. 2024, A&A, 683, A12
Meibom, S., Mathieu, R. D., & Stassun, K. G. 2009, ApJ, 695, 679
Meibom, S., Mathieu, R. D., Stassun, K. G., et al. 2011, ApJ, 733, 115
Metcalfe, T. S., van Saders, J. L., Pinsonneault, M. H., et al. 2025, ApJ, 991, L17
Mosser, B., Goupil, M. J., Belkacem, K., et al. 2012, A&A, 548, A10
Moyano, F. D., Eggenberger, P., Mosser, B., et al. 2023, A&A, 673, A110
Oglethorpe, R. L. F., & Garaud, P. 2013, ApJ, 778, 166
Pinsonneault, M. H., Kawaler, S. D., Sofia, S., et al. 1989, ApJ, 338, 424
Reiners, A., & Mohanty, S. 2012, ApJ, 746, 43
Ruediger, G., & Kitchatinov, L. L. 1996, ApJ, 466, 1078
Santos, A. R. G., Godoy-Rivera, D., Mathur, S., et al. 2025, A&A, 697, A177
Schatzman, E. 1962, Ann. Astrophys., 25, 18
Schou, J., Antia, H. M., Basu, S., et al. 1998, ApJ, 505, 390
Skumanich, A. 1972, ApJ, 171, 565
Somers, G., & Pinsonneault, M. H. 2016, ApJ, 829, 32
Spada, F., & Lanzafame, A. C. 2020, A&A, 636, A76
Spada, F., Lanzafame, A. C., Lanza, A. F., et al. 2011, MNRAS, 416, 447
Spada, F., Gellert, M., Arlt, R., et al. 2016, A&A, 589, A23
Stix, M. 1972, A&A, 20, 9
Taylor, B. J. 2007, AJ, 133, 370
van Saders, J. L., & Pinsonneault, M. H. 2012, ApJ, 751, 98
van Saders, J. L., & Pinsonneault, M. H. 2013, ApJ, 776, 67
van Saders, J. L., Ceillier, T., Metcalfe, T. S., et al. 2016, Nature, 529, 181
Van-Lane, P. R., Speagle, J. S., Eadie, G. M., et al. 2025, ApJ, 986, 59
Virtanen, P., Gommers, R., Oliphant, T. E., et al. 2020, Nat. Meth., 17, 261
Weber, E. J., & Davis, L. 1967, ApJ, 148, 217

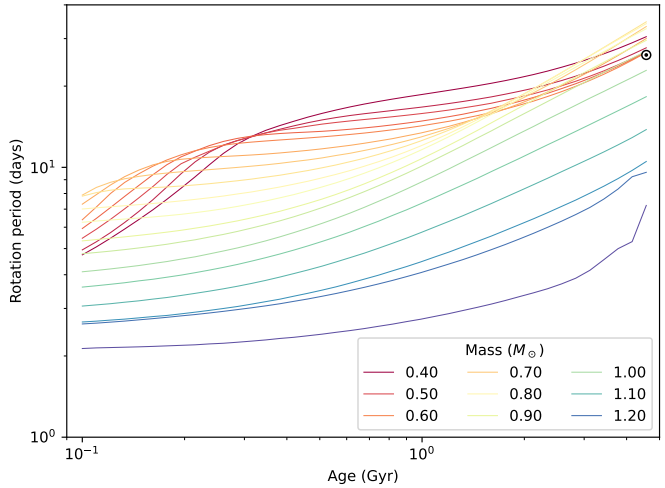

Fig. A.1. Evolution of slow–rotator sequence according to model "bpl": rotational history for models of selected mass.

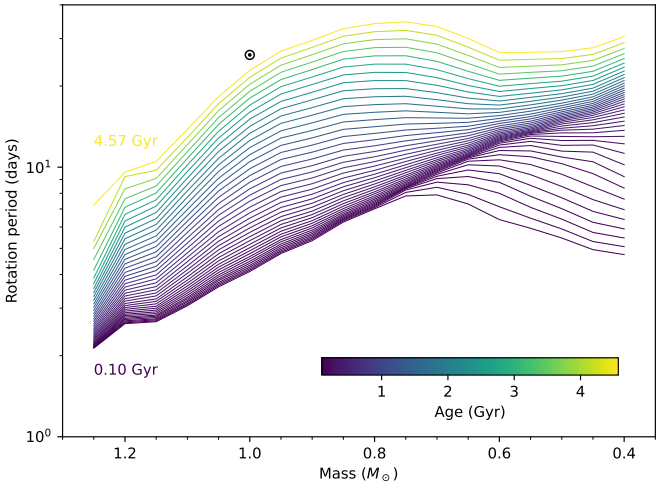

Fig. A.2. Evolution of slow–rotator sequence according to model "bpl": rotational isochrones from 0.1 to 4.57 Gyr.

Appendix A: Rotational isochrones

The Figures and the Table in this Appendix are meant to provide a qualitative and quantitative impression of the rotational evolution of the slow–rotator sequence according to model "bpl". The main features of the rotational isochrones discussed in this section are shared by those obtained with model "ienv". For a detailed description of these models, see Section 4.

Figure A.1 shows the evolution of the surface rotation period as a function of the stellar mass, which is the direct output of our model; the Sun is also plotted with its usual symbol. It should be noted that our models are not calibrated to reproduce the solar rotation period exactly. The model at 0.95 $M_\odot$ turns out to be the one closest to the solar period (26.09 days) at 4.57 Gyr. This is not surprising, since the solar rotation period was not included as a constraint in our fit.

Figure A.2 shows isochrones from 0.1 to 4.57 Gyr in the usual period vs. mass diagram. A piling up of the isochrones of age up to $\approx$ 2 Gyr is clearly visible, with stars of lower mass converging onto the ridge with increasingly longer timescale. This over-density of isochrones corresponds to a period of slowed down rotational evolution, and is a direct consequence of the stalled spin-down phase due to the resurfacing of angular momentum from the interior via the (mass-dependent) recoupling mechanism.

Figure A.3 shows a three-dimensional representation of the full mass–age–rotation period relation. This view illustrates how the rotation period depends on both stellar mass and age. It is clear, in particular, that the rotation period cannot be adequately represented by a functional relation in which the dependences on mass and age enter as separate, independent factors.

Table A.1 lists the surface rotation period as a function of age, with each column corresponding to a different stellar mass. In other words, each row is an isochrone, whose age is given by the first entry in the row. The de-reddened Gaia $(G_{BP} - G_{RP})_0$ color corresponding to each mass is also given in the bottom row for reference. For the purposes of the Table, the mass-to-color conversion has been performed using a MIST isochrone of solar metallicity and age equal to 1 Gyr.

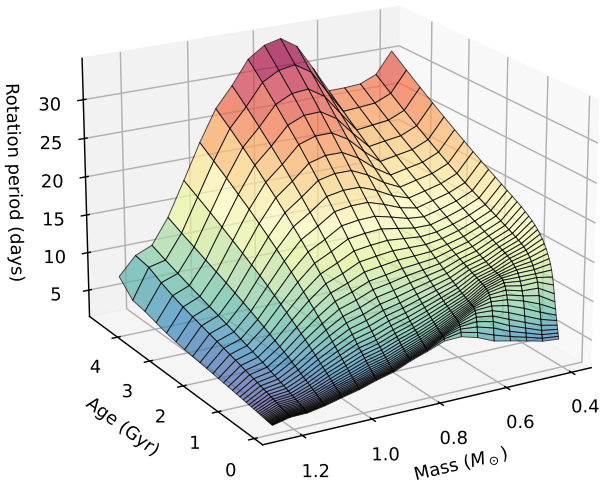

Fig. A.3. Evolution of slow–rotator sequence according to model "bpl": three-dimensional representation of mass–age–rotation period relation.

Table A.1. Rotational isochrones (rows) and rotational histories (columns) for stars on slow–rotator sequence according to "bpl" model. Units of age, mass, and rotation period are Gyr, $M_\odot$, and days, respectively.

Age	Mass																	
	0.40	0.45	0.50	0.55	0.60	0.65	0.70	0.75	0.80	0.85	0.90	0.95	1.00	1.05	1.10	1.15	1.20	1.25
0.10	4.74	4.95	5.46	5.93	6.39	7.30	7.89	7.82	7.01	6.26	5.34	4.78	4.10	3.60	3.06	2.67	2.63	2.13
0.11	5.20	5.43	6.06	6.67	7.42	8.14	8.56	8.13	7.10	6.34	5.42	4.85	4.17	3.66	3.10	2.70	2.65	2.14
0.13	5.75	6.06	6.81	7.56	8.54	9.04	8.99	8.30	7.19	6.42	5.50	4.93	4.24	3.72	3.15	2.73	2.69	2.15
0.15	6.40	6.86	7.70	8.56	9.46	9.77	9.26	8.37	7.27	6.49	5.60	5.03	4.33	3.80	3.20	2.77	2.72	2.16
0.17	7.17	7.85	8.78	9.67	10.29	10.33	9.45	8.42	7.37	6.57	5.70	5.13	4.43	3.87	3.26	2.81	2.76	2.17
0.19	8.10	9.12	10.04	10.72	10.97	10.66	9.60	8.50	7.48	6.67	5.81	5.26	4.54	3.96	3.33	2.86	2.80	2.18
0.21	9.22	10.48	10.91	11.49	11.53	10.83	9.72	8.61	7.61	6.79	5.95	5.39	4.66	4.07	3.41	2.91	2.85	2.20
0.24	10.56	11.64	11.67	12.19	11.93	10.92	9.84	8.73	7.75	6.94	6.10	5.55	4.81	4.19	3.50	2.97	2.90	2.22
0.28	11.91	12.43	12.40	12.70	12.21	11.01	9.96	8.88	7.92	7.12	6.29	5.74	4.98	4.33	3.60	3.04	2.96	2.24
0.31	13.02	12.97	13.00	13.05	12.40	11.11	10.10	9.05	8.11	7.33	6.50	5.96	5.18	4.49	3.71	3.11	3.02	2.27
0.36	13.91	13.56	13.52	13.27	12.56	11.23	10.26	9.25	8.34	7.57	6.74	6.20	5.40	4.67	3.85	3.20	3.09	2.30
0.41	14.63	14.11	13.88	13.41	12.70	11.39	10.45	9.47	8.59	7.85	7.02	6.49	5.66	4.87	3.99	3.30	3.17	2.34
0.46	15.35	14.64	14.21	13.51	12.85	11.56	10.65	9.73	8.88	8.18	7.35	6.81	5.95	5.12	4.17	3.41	3.25	2.38
0.52	16.00	15.09	14.53	13.63	13.01	11.77	10.91	10.05	9.23	8.56	7.73	7.19	6.29	5.38	4.36	3.54	3.36	2.42
0.60	16.61	15.48	14.80	13.80	13.19	12.01	11.20	10.39	9.63	9.00	8.18	7.62	6.68	5.69	4.57	3.69	3.47	2.47
0.68	17.16	15.80	15.04	14.00	13.40	12.28	11.55	10.81	10.10	9.51	8.68	8.13	7.11	6.03	4.81	3.85	3.59	2.53
0.77	17.66	16.09	15.28	14.23	13.64	12.60	11.94	11.29	10.64	10.10	9.27	8.69	7.60	6.42	5.09	4.03	3.74	2.59
0.87	18.14	16.39	15.53	14.51	13.92	12.98	12.40	11.86	11.27	10.79	9.95	9.34	8.17	6.86	5.39	4.23	3.89	2.66
0.99	18.59	16.70	15.81	14.83	14.23	13.40	12.95	12.53	12.01	11.58	10.72	10.07	8.80	7.33	5.73	4.46	4.07	2.74
1.13	19.06	17.05	16.13	15.21	14.62	13.91	13.59	13.30	12.86	12.49	11.59	10.89	9.49	7.88	6.11	4.72	4.27	2.82
1.28	19.54	17.44	16.50	15.62	15.04	14.51	14.35	14.21	13.86	13.54	12.59	11.81	10.26	8.46	6.51	5.00	4.49	2.92
1.45	20.06	17.87	16.92	16.14	15.54	15.19	15.23	15.27	15.01	14.72	13.69	12.83	11.13	9.10	6.97	5.31	4.74	3.03
1.65	20.64	18.38	17.42	16.70	16.13	15.99	16.26	16.50	16.35	16.06	14.93	13.95	12.05	9.83	7.48	5.66	5.03	3.15
1.87	21.31	18.98	18.05	17.37	16.80	16.93	17.48	17.92	17.86	17.55	16.30	15.16	13.07	10.59	8.02	6.03	5.35	3.28
2.13	22.07	19.65	18.74	18.16	17.60	18.05	18.90	19.57	19.55	19.21	17.78	16.48	14.17	11.44	8.63	6.45	5.70	3.43
2.42	22.98	20.51	19.58	19.05	18.55	19.36	20.55	21.45	21.47	21.02	19.41	17.92	15.38	12.36	9.28	6.91	6.10	3.60
2.75	24.05	21.49	20.58	20.12	19.67	20.89	22.48	23.55	23.56	23.01	21.16	19.47	16.65	13.35	9.99	7.43	6.55	3.81
3.12	25.29	22.68	21.77	21.39	21.00	22.69	24.69	25.91	25.88	25.17	23.03	21.13	18.05	14.41	10.78	8.02	7.10	4.15
3.54	26.74	24.09	23.16	22.88	22.57	24.79	27.22	28.55	28.38	27.48	25.06	22.95	19.51	15.59	11.65	8.70	7.83	4.72
4.02	28.47	25.75	24.83	24.63	24.43	27.22	30.08	31.44	31.14	29.93	27.24	24.88	21.14	16.87	12.63	9.51	8.91	5.00
4.57	30.49	27.73	26.84	26.68	26.65	30.03	33.25	34.62	34.09	32.62	29.56	26.94	22.88	18.28	13.80	10.51	9.58	7.22
	2.08	1.98	1.88	1.78	1.66	1.51	1.36	1.24	1.13	1.02	0.93	0.87	0.80	0.75	0.71	0.66	0.62	0.58
Age	$(G_{BP} - G_{RP})_0$																	